

Plasma-Catalytic Ammonia Synthesis beyond Thermal Equilibrium on Ru-based Catalysts in Non-thermal Plasma

Supporting Information

Kevin H. R. Rouwenhorst* ^[a], Hugo G. B. Burbach ^[a], Dave W. Vogel ^[b], Judit Núñez Paulí ^[a], Bert Geerdink ^[a], and Leon Lefferts* ^[a]

[a] ir. K.H.R. Rouwenhorst, Prof. dr. ir. L. Lefferts
Catalytic Processes & Materials
MESA+ Institute for Nanotechnology, University of Twente
P.O. Box 217, 7500 AE Enschede (The Netherlands)
E-mail: k.h.r.rouwenhorst@utwente.nl, l.lefferts@utwente.nl

[b] University of Twente
Current address: Breemarsweg 248, 7553 HW, Hengelo (The Netherlands)

Contents

S.1 Experimental procedure	2
S1.1 Materials.....	2
S1.2 Catalyst preparation	2
S1.3 Catalyst characterization	2
S1.4 Plasma characterization.....	2
S1.5 Catalytic tests	3
S2 Results	3
S2.1 Catalyst characterization	3
S2.2 Plasma characterization.....	4
S2.3 Thermal catalysis	6
S2.4 Plasma-catalysis beyond thermal equilibrium.....	7
S3 Discussion	8
S3.1 Kinetic diameter	8
S3.2 Modelled and experimental plasma-catalytic conversion.....	8
Fitting the reactor dimensions	8
Plasma-activation in N ₂	9
References.....	12

S.1 Experimental procedure

Ru/MgO catalysts were tested for the activity for ammonia synthesis in the absence and in the presence of a plasma, as ruthenium-based catalysts are most active for ammonia synthesis under mild conditions [1]. Furthermore, ruthenium-based catalysts have been studied most among transition metals for the plasma-catalytic activity [2–8]. The MgO support was chosen because of the absence of acid sites, and the high thermal activity for ammonia synthesis [9]. Acid sites on supports such as Al₂O₃ cause ammonia desorption limitations at mild temperatures (<200°C) [10], making the distinction between desorption limitations of an active metal and the support difficult. Furthermore, a potassium alkali promoter is added to enhance the ammonia synthesis [1, 11, 12]. The potassium promoter enhances the activity for N₂ dissociation and the rate of ammonia desorption [3, 11, 12].

S1.1 Materials

Ruthenium (III) nitrosyl nitrate (Ru(NO)(NO₃)₃, >31.3 wt.% Ru) was purchased from Alfa Aesar. Magnesium oxide (MgO, >97% purity grade, 30 m² g⁻¹) and potassium nitrate (KNO₃, 99% purity grade) were purchased from Merck. H₂ and N₂ with a purity grade of 99.999% were purchased from Linde, and water traces were removed using Agilent gas clean purification systems. A gas mixture of 2 vol.% NH₃ in a 98 vol.% N₂ balance gas was purchased from Linde. All materials were used as received. Deionized water was used during catalyst preparation.

S1.2 Catalyst preparation

The Ru(NO)(NO₃)₃ precursor was dissolved in water and impregnated on the MgO support using the dry impregnation method. About 1.2 mL⁻¹ water was used per gram of MgO. Then, the mixture was dried in an oven at 100°C and atmospheric pressure for 1 h, followed by drying in a vacuum oven at 120°C for 2 h.

The dried catalyst was calcined in 20 mL min⁻¹ air flow at 400°C for 2 h in order to oxidize the Ru precursor. Subsequently, the RuO₂ was reduced in a 20 mL min⁻¹ H₂ flow at 400°C for 2.5 h. For the Ru-K/MgO catalyst, KNO₃ was dissolved in water and impregnated on the Ru/MgO catalyst, using the dry impregnation method. About 1.2 mL⁻¹ water was used per gram of Ru/MgO. Then, the mixture was dried in an oven at 100°C and atmospheric pressure for 1 h, followed by drying in a vacuum oven at 120°C for 2 h. After reduction, the catalysts were pelletized and crushed. The sieve fraction 250-300 μm was used for the catalytic tests. Last traces of H₂O and nitrates are removed in the reactor at 400°C.

S1.3 Catalyst characterization

The total surface area and pore volume was determined by N₂ chemisorption at -198°C using a Micromeritics Tristar. The samples were outgassed in vacuum at 300°C for 24 h before the analysis. The Ru particle size and metal dispersion were determined by CO chemisorption. The elemental composition was determined by x-ray fluorescence spectroscopy (XRF) using Bruker S8 tiger. The crystalline phases present in the catalyst, as well as the Ru particle sizes were determined with x-ray diffraction (XRD) using a Bruker D2 Phaser diffractometer equipped with a position-sensitive detector over a 2θ range between 10° and 90° using Cu Kα radiation (λ= 1.5418 Å). Particles sizes of Ru are estimated based on the width of the peak at 38° using the Scherrer equation.

S1.4 Plasma characterization

A PMV 500-4000 power supply was used to illuminate the plasma at 25 kHz. A Picoscope PC Oscilloscope was used to monitor the charge-voltage characteristics. The high voltage electrode was connected to the power supply, and an AC voltage of up to 10 kV peak to peak was applied. A Tektronix P6015A high voltage probe was used to monitor the voltage over the high voltage electrode, while a TT-HV 250 voltage probe was used to measure the voltage over the ground electrode. A capacitor of

8.24 nF was placed in between the ground electrode and the TT-HV 250 voltage probe. An Ocean HDX Spectrometer was used to analyze light emitted by the plasma, just below the catalyst bed, at low temperature.

S1.5 Catalytic tests

A schematic representation of the experimental set-up for the catalytic tests is shown in Figure S1. The catalytic tests were carried out in a quartz tubular reactor with an inner diameter of 4 mm and an outer diameter of 6 mm, at atmospheric pressure. A stainless-steel rod of 1 mm diameter is placed inside the reactor as the high voltage electrode. At the outside of the quartz tube, a metal tube is placed as the ground electrode. The temperature was controlled with a thermocouple connected to a heating block, which is placed around the ground electrode. The flowrates of the reactants were controlled with calibrated mass flow controllers (MFCs). Typically, 130 mg of catalyst with particle size 250-300 μm was loaded in the reactor, on top of a layer of quartz wool. A spacer is placed above the catalytic bed to prevent moving of particles due to plasma-illumination and to center the high voltage electrode.

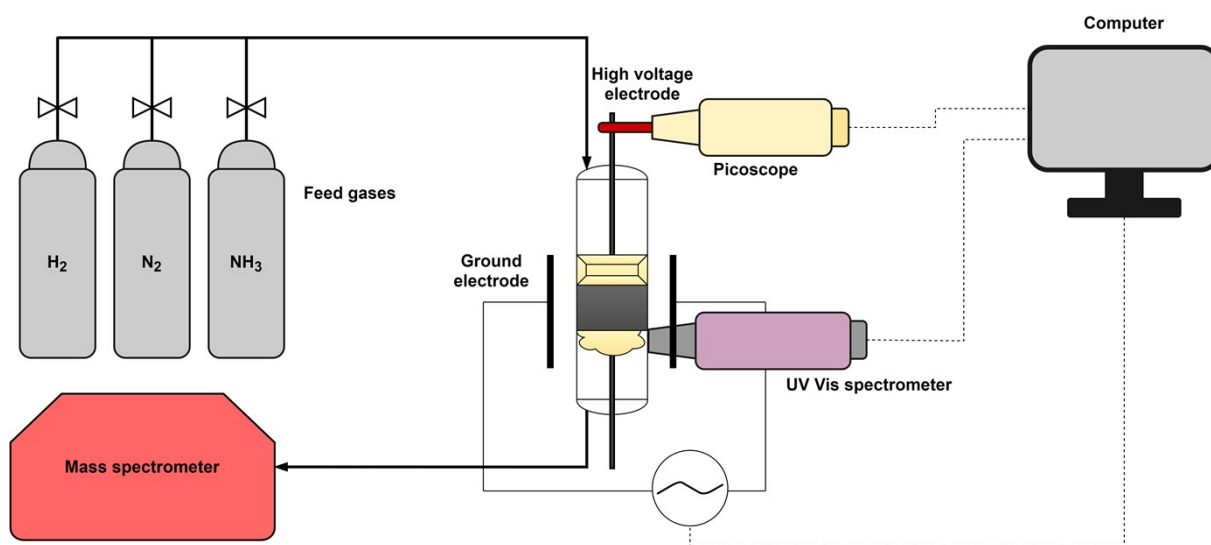


Figure S1: Schematic representation of the experimental set-up. The plasma volume includes the space, the packed bed, and the quartz wool.

The catalyst was reduced at 400°C in the reactor for 2 h in a gas mixture of 40 mL min⁻¹ N₂ and 10 mL min⁻¹ H₂. The catalytic tests were performed in a temperature-programmed plasma surface reaction, as previously reported by Parastaev et al. [13]. The heating rate was 2.5 K min⁻¹, which is sufficiently slow such that the temperature ramp approaches a steady-state at a given temperature. The product gases were analyzed using an on-line Pfeiffer Vacuum ThermoStar™ gas analysis system, which is a mass spectrometer (MS). The MS signal for NH₃ (17 m/e) was calibrated in the range 0-2 mol.%, resulting in a linear relationship. The signals for H₂ (2 m/e), N₂ (28 m/e) and H₂O (18 m/e) were also monitored semi-quantitatively, as well as a minor NH₃ peak (16 m/e).

S2 Results

S2.1 Catalyst characterization

The catalyst characterization results for MgO, Ru/MgO, and Ru-K/MgO are listed in Table S1. The XRD spectrum of Ru/MgO is shown in Figure S2. The results are in line with previously reported data [9, 14, 15].

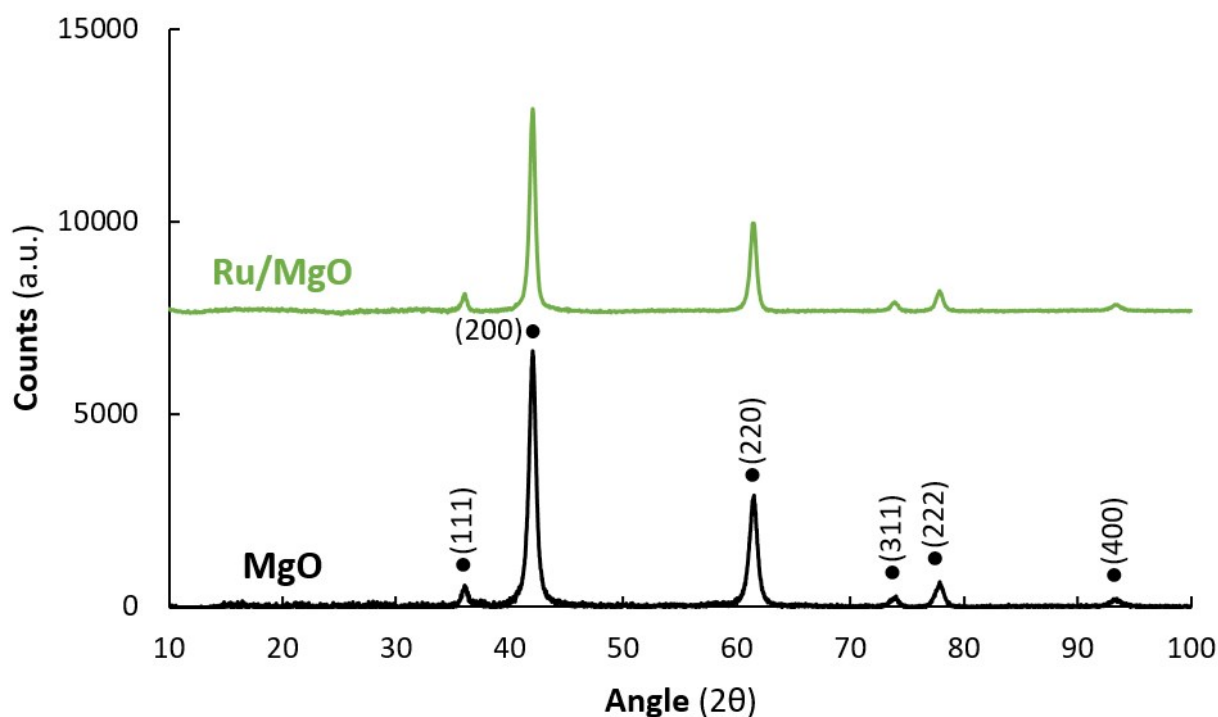


Figure S2: XRD spectrum for MgO and Ru/MgO. The Miller indices indicate the crystalline lattice structures exposed in the MgO.

Table S1: Structural and physical properties of MgO, Ru/MgO, and Ru-K/MgO. ^a Measured with N₂ physisorption. ^b Determined by XRF. ^c Determined by CO chemisorption. ^d Determined by XRD-LB.

Catalyst	S _{BET} (m ² g ⁻¹) ^a	V _{Pore} (cm ³ g ⁻¹) ^a	Ru loading (wt.%) ^b	K loading (wt.%) ^b	Ru particle size (nm) ^c	Ru dispersion (%) ^c
MgO	294	0.31	-	-	-	-
Ru/MgO	78	0.21	2.0	-	16 ^c , 15 ^d	9.2
Ru-K/MgO	-	-	1.9	6.1	16 ^c , 15 ^d	9.2

S2.2 Plasma characterization

The voltage and charge were monitored with an oscilloscope, from which the power dissipated can be determined using a Lissajous figure. An example of a Lissajous figure (also termed Q-V plot) is shown in Figure S3. In a Q-V plot, the capacitive and discharge behavior of a plasma is monitored. Ideally, a Lissajous figure has the shape of a parallelogram, thereby perfectly separating the capacitive and discharge regime. However, as shown in Figure S3, there is an indent in both the positive and negative charge cycle. This can be attributed to a discharge at the contact points at an earlier stage than over the remainder of the surface [16, 17]. The choice of the packing had little to no influence on the discharge characteristics, in line with literature data reported by Herrera et al. [16].

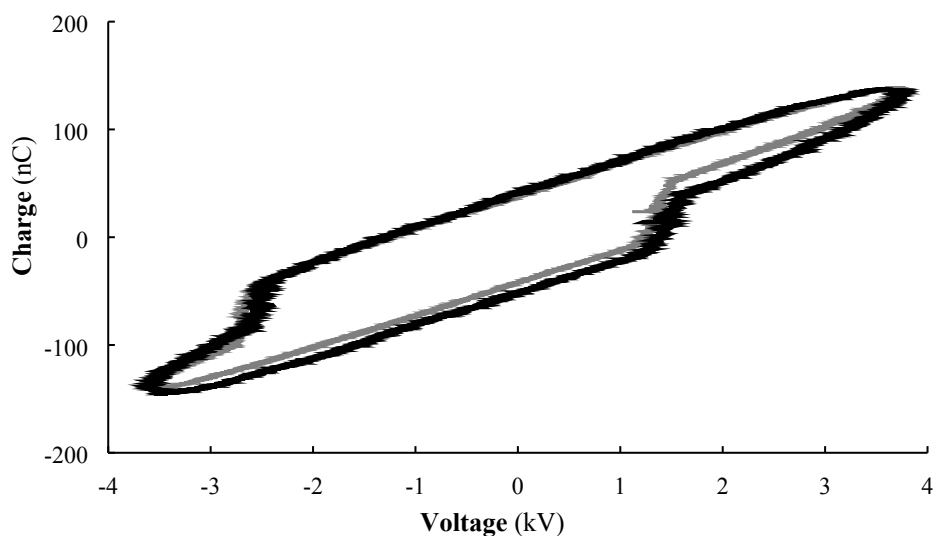
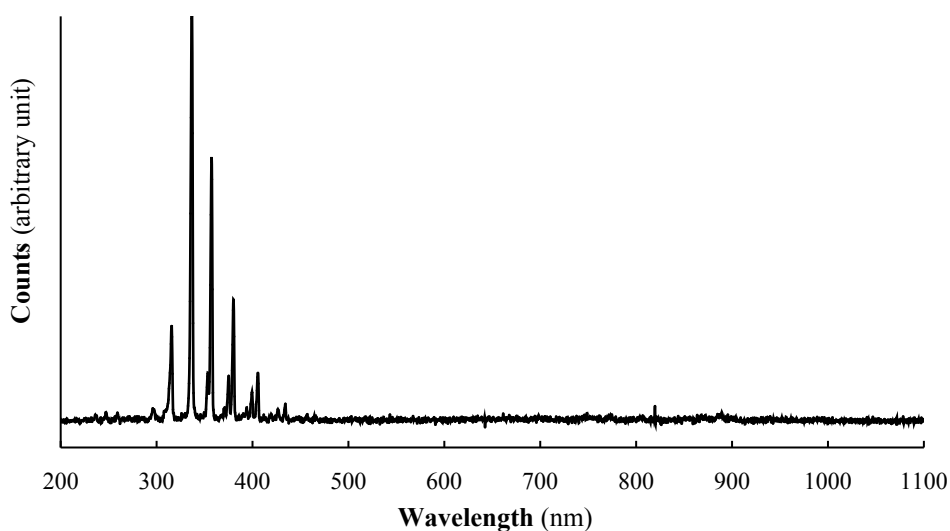
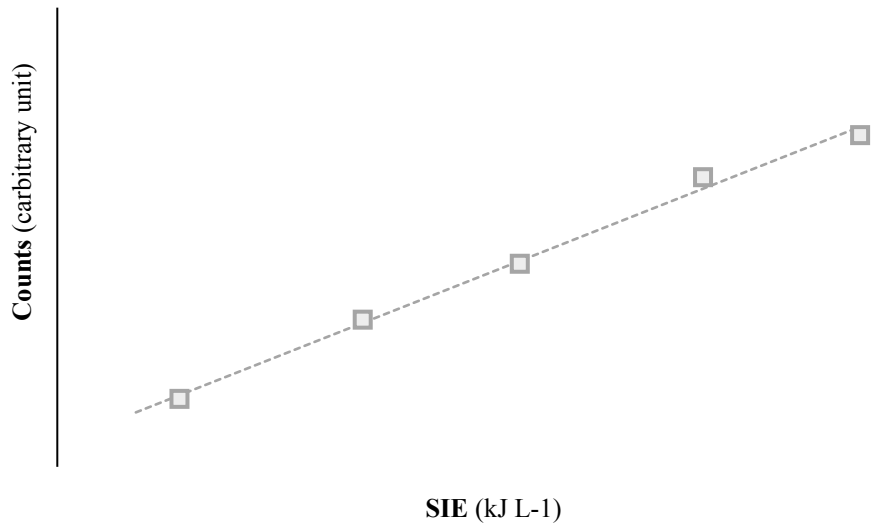


Figure S3: Lissajous figure for MgO (grey) and Ru-K/MgO (black) at 30°C, H₂:N₂=1:1, 20 mL min⁻¹. The total power dissipated is 6.4 W.

An example of an emission spectrum at 6.4 W input power and in pure N₂ is shown in Figure S4, in line with literature [15, 18]. As follows from the emission spectrum, the most pronounced peaks are found in the regime 290-400 nm, which corresponds to the second positive band from an activated neutral N₂^{*} molecule (C³Π_u → B³Π_g) [19]. This implies that photons are emitted upon plasma-activated N₂ falling back from an electronically and/or vibrationally excited state to a lower energy state of N₂.



a.



b.

Figure S4: a. Number of counts for pure N₂, measured in quartz wool just below MgO packing at SIE=19.2 kJ L⁻¹. Flowrate 10 mL min⁻¹. b. Number of counts of UV Vis spectrum at 337 nm (Transition from N₂(C³Π_u(v=0)) to N₂(B³Π_g(v=0)), □ grey squares), as function of the SIE.

S2.3 Thermal catalysis

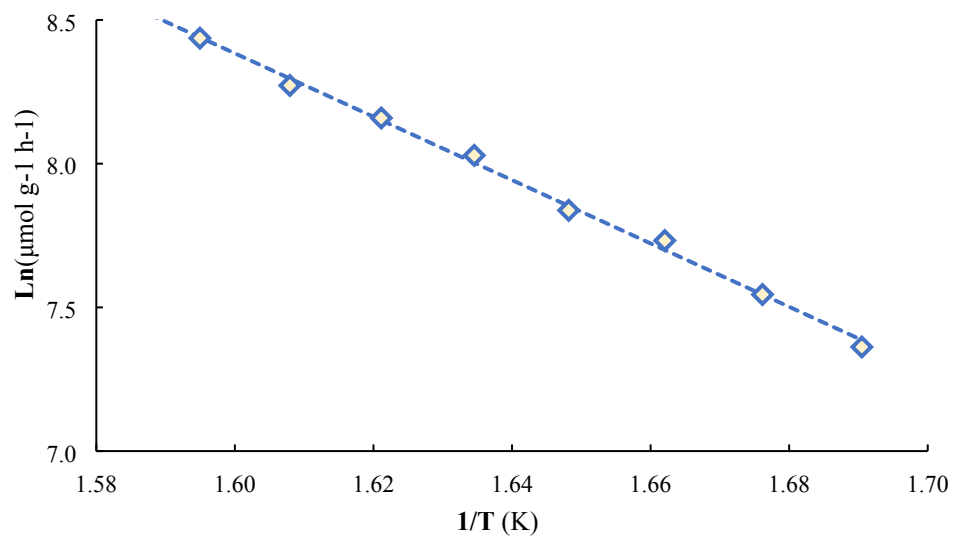


Figure S5: Arrhenius plot for thermal-catalytic NH₃ synthesis over Ru-K/MgO. Total flowrate 20 mL min⁻¹, H₂:N₂=1:1, catalyst loading 130 mg (250-300 μm), 0.0 mol.% NH₃ co-feed. The calculated activation barrier is 92 kJ mol⁻¹.

S2.4 Plasma-catalysis beyond thermal equilibrium

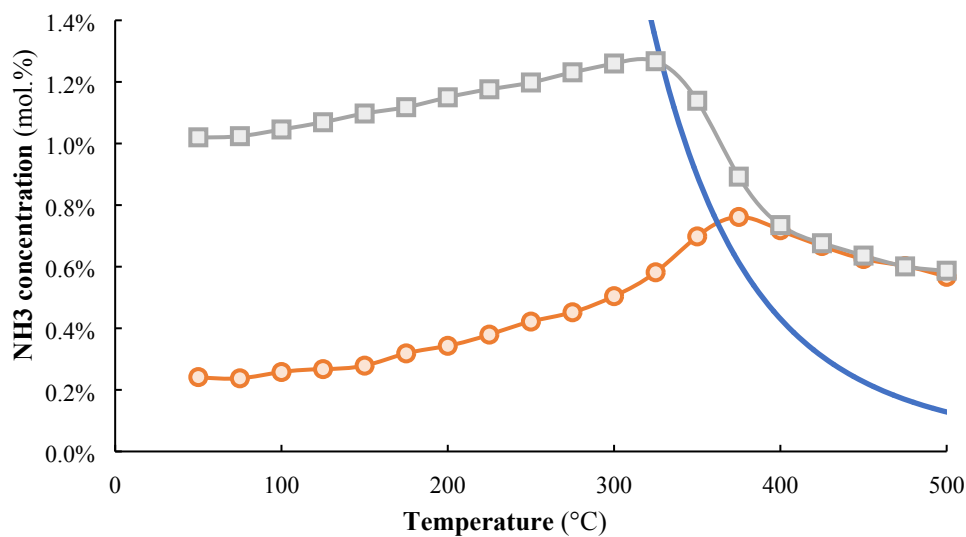


Figure S6: Activity for plasma-catalytic NH₃ synthesis (and NH₃ decomposition) for Ru-K/MgO for various NH₃ co-feed concentrations (0.0 mol.% (orange circles) and 1.0 mol.% (grey squares)). Total flowrate 20 mL min⁻¹, H₂:N₂=1:1, catalyst loading 130 mg (250-300 μm), plasma power 4.8 W (SIE=14.4 kJ L⁻¹).

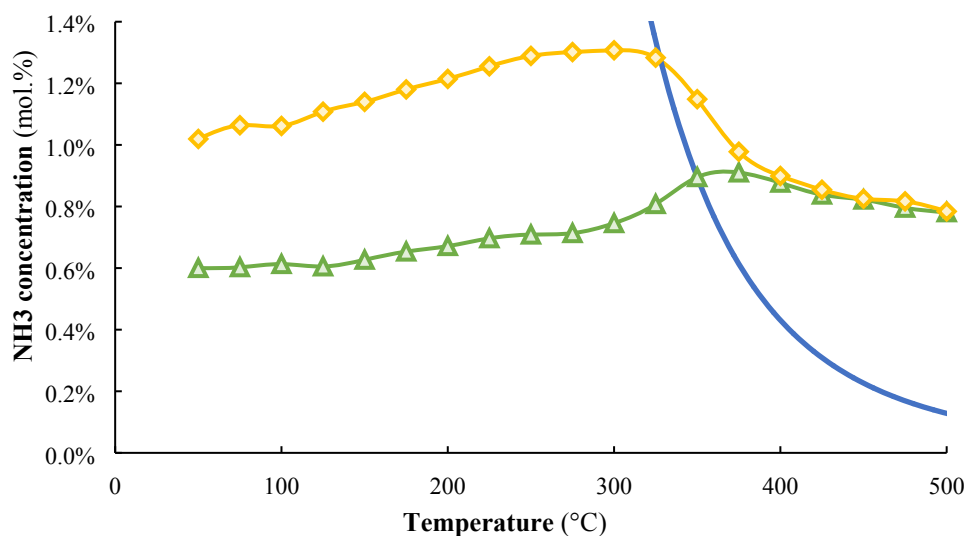


Figure S7: Activity for plasma-catalytic NH₃ synthesis (and NH₃ decomposition) for Ru-K/MgO for various NH₃ co-feed concentrations (0.0 mol.% (green triangles) and 1.0 mol.% (yellow diamonds)). Total flowrate 20 mL min⁻¹, H₂:N₂=1:1, catalyst loading 130 mg (250-300 μm), plasma power 6.4 W (SIE=19.2 kJ L⁻¹).

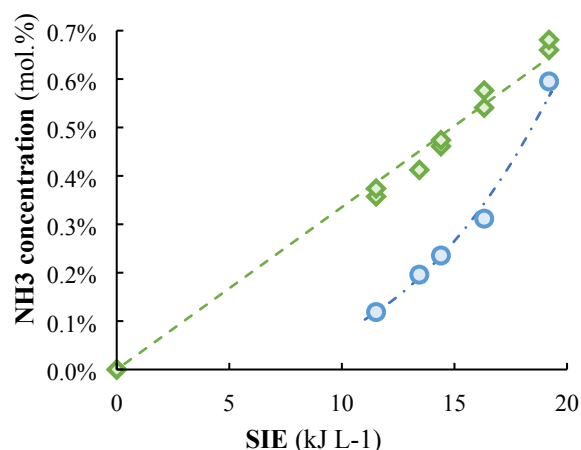


Figure S8: Ammonia outlet concentration as function of the SIE at 50°C (plasma-chemistry only, blue circles) and the difference between the thermal equilibrium and the conversion at 450-500°C (equilibrium conversion, green diamonds) over Ru-K/MgO.

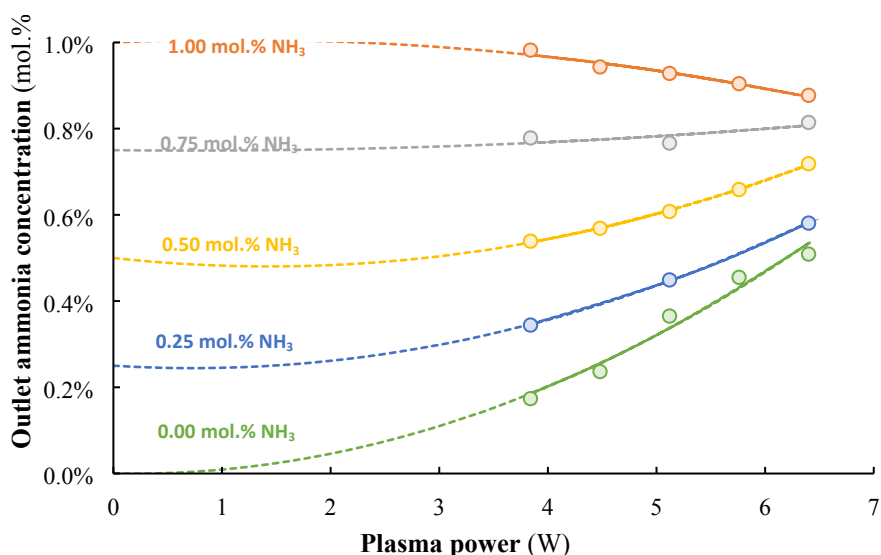


Figure S9: Effect of the plasma power on the activity for plasma-chemical NH₃ synthesis for MgO at ambient conditions, with various NH₃ co-feeding concentrations. Temperature 250°C, total flowrate 20 mL min⁻¹, H₂:N₂=1:1, catalyst loading 150 mg (250-300 μm particles). The plasma power applied under most conditions is 3.8 W.

S3 Discussion

S3.1 Kinetic diameter

- **Ammonia (ground state):** 260 pm
- **Hydrogen (ground state):** 289 pm
- **Nitrogen (ground state):** 364 pm

S3.2 Modelled and experimental plasma-catalytic conversion

In order to model the plasmas-catalytic conversion over Ru-based catalysts, the model of Mehta et al. [20] was used without modifications to the source code. The source code was made openly available by Mehta et al. [20]. The authors estimated activities for NH₃ synthesis and NH₃ decomposition, based on a kinetic model. In this model, the N₂ activation barrier is the key descriptor, while the

hydrogenation steps are lumped. Plasma-activation is assumed to lower the barrier for N_2 dissociation and therefore increase the rate of N_2 dissociation. However, the final state of adsorbed N_{ads} on the surface is assumed to be the same for dissociated ground-state N_2 and plasma-activated N_2 and only the concentration of N_{ads} is influenced.

Fitting the reactor dimensions

All experiment in our research (both for thermal catalysis and plasma catalysis) were performed at 20 mL min^{-1} with a $H_2:N_2$ ratio of 1:1, with a catalyst mass of 130 mg and a bed volume of 0.14 cm^3 . The CO chemisorption results for Ru/MgO give an area of $0.712 \text{ m}^2 \text{ g}^{-1}$, resulting in a site density of approximately $6.5 \cdot 10^{-6} \text{ mol cm}^{-3}$.

For using the model for Ru-K/MgO catalyst, a N binding energy of -0.3 eV is assumed, based on the binding energy reported for Ru(0001) at 0.25 ML coverage [21]. Similar coverages were found for microkinetic models of promoted Ru catalysts [22]. The potassium promoter has little to no influence on the N binding energy [23, 24], implying $E_N = -0.3 \text{ eV}$ is used for Ru-K/MgO.

The experimental results for thermal-catalytic ammonia synthesis over Ru-K/MgO (Figure 2) are used to fit the model of Mehta et al. This results in an underestimation of the experimental data of four orders of magnitude for a site density of $6.5 \cdot 10^{-6} \text{ mol cm}^{-3}$, i.e. the approximate site density for the used catalyst. An underestimation is more often reported for kinetic models (although not of this magnitude), which is due to the methods used for the generalized gradient approximation in microkinetic models [25]. In order to fit the model to our observations, the site density was increased to $5.0 \cdot 10^{-2} \text{ mol cm}^{-3}$ keeping all other physical parameters constant. As shown in Figure S10, the trends in the kinetic regime ($300\text{-}380^\circ\text{C}$) predicted by the adjusted model agree well with experimental observations. Thus, the model parameters used for Figure S10 are also used to predict plasma-catalytic ammonia synthesis.

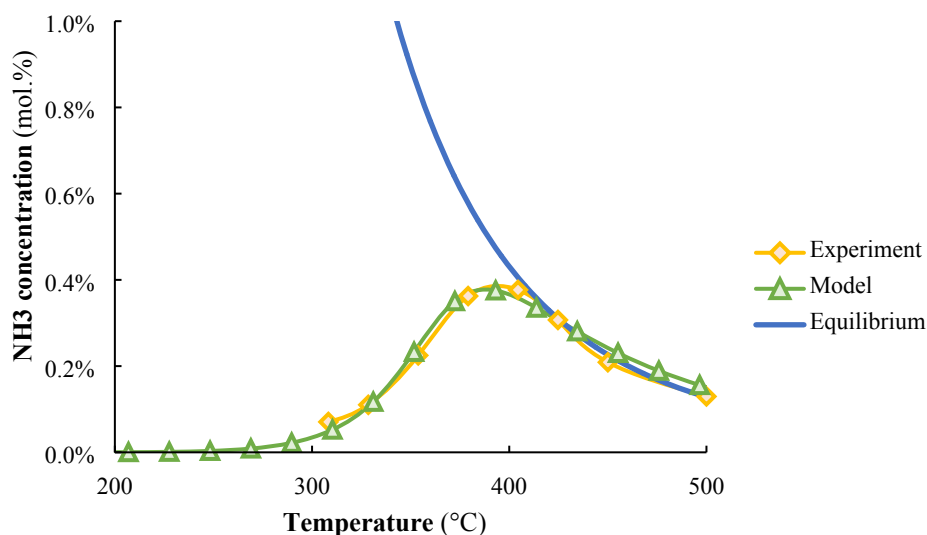


Figure S10: Experimental (orange line) and predicted (blue line) thermal-catalytic NH_3 conversion over Ru-K/MgO as function of temperature. Total flowrate 20 mL min^{-1} , $H_2:N_2=1:1$ (no NH_3 co-feed), catalyst loading 130 mg (250-300 μm). The N binding energy is assumed to be -0.3 eV , based on a Ru(0001) at 0.25 ML coverage [21].

Plasma-activation in N_2

Plasma-activation lowers the barrier for N_2 dissociation [3], as well as the N_2 dissociation probability [26, 27]. The plasma-activation is assumed to lower the N_2 dissociation barrier by 0.7 eV. This is based on the difference between the apparent activation barriers calculated for thermal catalysis and plasma-catalysis over promoted Ru-catalysts, which can be attributed to the lower N_2 dissociation barrier [3].

Various values for the lowering of the N_2 dissociation barrier are shown in Figure S11. When N_2 is only partially activated in the plasma and the catalyst is required for dissociation (i.e., for low plasma-activations (of <0.5 eV)), the kinetic model of Mehta et al. predicts that there is no NH_3 formation below $200^\circ C$ due to the negligible rate of N_2 dissociation. Only when the plasma-activation is above the N_2 dissociation barrier on Ru (according to the model 1.0 eV), NH_3 formation is predicted below $200^\circ C$. The fact that NH_3 is only formed when the N_2 barrier is completely overcome by the plasma, indicates that NH_3 formation from NH_x radicals or highly activated N_2 is the dominant mechanism for NH_3 synthesis below $200^\circ C$, as was experimentally observed below $200^\circ C$ (see Figure 3). It should be noted that the dissociative sticking probability of N_2 on Ru(0001) is far below 100% in reality for a plasma-activation of 1.0 eV [27], which is not incorporated in the model of Mehta et al.

The model of Mehta et al. does not predict a change in conversion at high temperatures on increasing the level of activation from 0.5 eV to 1.0 eV. This is not expected, as an increase of plasma-activated N_2 on the surface should boost the plasma-catalytic ammonia synthesis reaction according to our experimental results (see Figure 7 and Figure 8 in the main article).

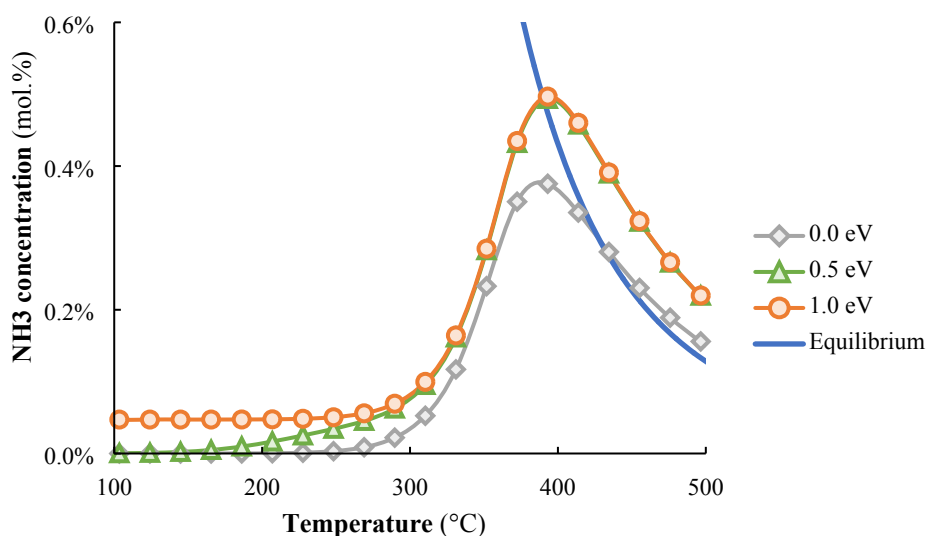


Figure S11: Predicted plasma-catalytic NH_3 conversion over Ru as function of temperature, based on the same reactor configuration as in Figure S9 (i.e., total flowrate 20 mL min^{-1} , $H_2:N_2=1:1$ (no NH_3 co-feed), catalyst loading 130 mg ($250\text{-}300 \mu\text{m}$)). The N binding energy is assumed to be -0.3 eV based on a Ru(0001) at 0.25 ML coverage [21] and $k_e n_e$ is assumed to be 10^{-3} ; the same value was used by Mehta et al. [20]. Various values for a decrease in N_2 dissociation barrier are assumed (0.0 eV , 0.5 eV , and 1.0 eV).

In Figure S12, we show the predicted influence of the N binding energy on the plasma-catalytic conversion to ammonia. The N binding energy is varied to get an estimate of the effect on the conversion beyond thermal equilibrium, as it is probable that the N_2 adsorption rate increases upon increasing plasma-activation of N_2 . The N binding energy on Ru is known to decrease with increasing

coverage [21, 24]. For instance, the N binding energy increases from -0.3 eV at 0.25 monolayer coverage to 0.9 eV at 1.00 monolayer coverage on Ru(0001) [21].

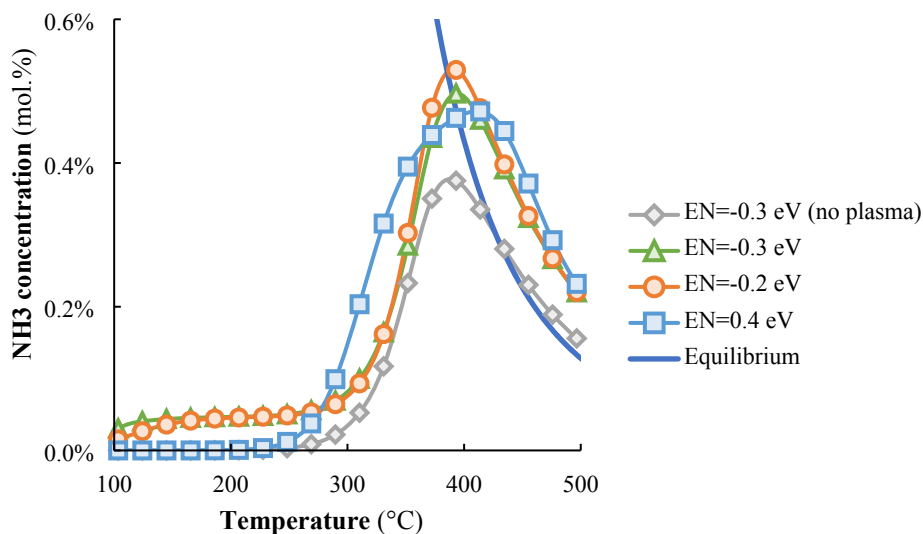


Figure S12: Predicted plasma-catalytic NH_3 conversion over Ru as function of temperature, based on the same reactor configuration as in Figure S9. The N binding energy is varied, while the barrier decrease is assumed to be 0.7 eV, based on experimental results obtained by Rouwenhorst et al. [3] for Ru catalysts. $k_e n_e$ is assumed to be 10^{-3} , similar to values used by Mehta et al. [20]. Various values for site densities are assumed to get similar conversion patterns: $5.0 \cdot 10^{-2} \text{ mol cm}^{-3}$ for $E_N = -0.3 \text{ eV}$, $1.0 \cdot 10^0 \text{ mol cm}^{-3}$ for $E_N = -0.2 \text{ eV}$, and $1.0 \cdot 10^4 \text{ mol cm}^{-3}$ for $E_N = 0.3 \text{ eV}$.

As shown in Figure S12, the model of Mehta et al. [20] predicts a variation in the plasma enhancement below 450°C, depending on the N binding strength. However, the model does not predict a change in conversion above 450°C with the N binding strength. This is not in line with our proposed model (see Figure 7 and Figure 8 in the main article) and experiment (see Figure 4 and Figure 5 in the main article).

Concluding, the model of Mehta et al. [20] is a first step in understanding the effect of plasma-activation on the effective barrier for N_2 dissociation and the subsequent NH_3 synthesis rate. At low temperatures (Figure S11), the model of Mehta et al. provides insight in the role of plasma-activated molecular N_2 and the adsorption of N radicals. However, above 450°C and beyond equilibrium, the model does not predict a variation in conversion to ammonia for different plasma powers, an effect that was experimentally observed (see Figure 8).

References

1. Liu, H. (2013). *Ammonia Synthesis Catalysts: Innovation and Practice*. World Scientific. doi:10.1142/8199
2. Li, S., van Raak, T., & Gallucci, F. (2020). Investigating the operation parameters for ammonia synthesis in dielectric barrier discharge reactors. *Journal of Physics D: Applied Physics*, *53*(1). doi:10.1088/1361-6463/ab4b37
3. Rouwenhorst, K. H. R., Kim, H.-H., & Lefferts, L. (2019). Vibrationally excited activation of N₂ in plasma-enhanced catalytic ammonia synthesis: a kinetic analysis. *ACS Sustainable Chemistry & Engineering*, *7*(20), 17515–17522. doi:10.1021/acssuschemeng.9b04997
4. Kim, H.-H., Teramoto, Y., Ogata, A., Takagi, H., & Nanba, T. (2017). Atmospheric-pressure nonthermal plasma synthesis of ammonia over ruthenium catalysts. *Plasma Processes and Polymers*, *14*(6), 1–9. doi:10.1002/ppap.201600157
5. Peng, P., Li, Y., Cheng, Y., Deng, S., Chen, P., & Ruan, R. (2016). Atmospheric Pressure Ammonia Synthesis Using Non-thermal Plasma Assisted Catalysis. *Plasma Chemistry and Plasma Processing*, *36*(5), 1201–1210. doi:10.1007/s11090-016-9713-6
6. Peng, P., Cheng, Y., Hatzenbeller, R., Addy, M., Zhou, N., Schiappacasse, C., ... Ruan, R. (2017). Ru-based multifunctional mesoporous catalyst for low-pressure and non-thermal plasma synthesis of ammonia. *International Journal of Hydrogen Energy*, *42*(30), 19056–19066. doi:10.1016/j.ijhydene.2017.06.118
7. Barboun, P. M., Mehta, P., Herrera, F., Go, D. B., Schneider, W. F., & Hicks, J. C. (2019). Distinguishing Plasma Contributions to Catalyst Performance in Plasma-Assisted Ammonia Synthesis. *ACS Sustainable Chemistry & Engineering*, *7*(9), 8621–8630. doi:10.1021/acssuschemeng.9b00406
8. Xie, Q., Zhuge, S., Song, X., & Lu, M. (2019). Non-thermal atmospheric plasma synthesis of ammonia in a DBD reactor packed with various catalysts. *Journal of Physics D: Applied Physics*, *53*(6). doi:10.1088/1361-6463/ab57e5
9. Aika, K., Takano, T., & Murata, S. (1992). Preparation and characterization of chlorine-free ruthenium catalysts and the promoter effect in ammonia synthesis. 3. A magnesia-supported ruthenium catalyst. *Journal of Catalysis*, *136*(1), 126–140. doi:10.1016/0021-9517(92)90112-U
10. Wang, Y., Craven, M., Yu, X., Ding, J., Bryant, P., Huang, J., & Tu, X. (2019). Plasma-Enhanced Catalytic Synthesis of Ammonia over a Ni/Al₂O₃ Catalyst at Near-Room Temperature: Insights into the Importance of the Catalyst Surface on the Reaction Mechanism. *ACS Catalysis*, *9*, 10780–10793. doi:10.1021/acscatal.9b02538
11. Ertl, G. (2009). Mechanisms of Heterogeneous Catalysis. In *Reactions at Solid Surfaces* (1st ed., pp. 123–139). Hoboken (NJ): John Wiley & Sons, Inc.
12. Aika, K.-I. (2017). Role of alkali promoter in ammonia synthesis over ruthenium catalysts—Effect on reaction mechanism. *Catalysis Today*, *286*, 14–20. doi:10.1016/j.cattod.2016.08.012
13. Parastaev, A., Hoeben, W. F. L. M., van Heesch, B. E. J. M., Kosinov, N., & Hensen, E. J. M. (2018). Temperature-programmed plasma surface reaction: An approach to determine plasma-catalytic performance. *Applied Catalysis B: Environmental*, *239*, 168–177. doi:10.1016/j.apcatb.2018.08.011
14. Muhler, M., Rosowski, F., Hinrichsen, O., Hornung, A., & Ertl, G. (1996). Ruthenium as catalyst for ammonia synthesis. *Studies in Surface Science and Catalysis*, *101*, 317–326.

doi:10.1016/S0167-2991(96)80242-4

15. Mehta, P., Barboun, P., Herrera, F. A., Kim, J., Rumbach, P., Go, D. B., ... Schneider, W. F. (2018). Overcoming ammonia synthesis scaling relations with plasma-enabled catalysis. *Nature Catalysis*, *1*(4), 269–275. doi:10.1038/s41929-018-0045-1
16. Herrera, F., Brown, G. H., Barboun, P., Turan, N., Mehta, P., Schneider, W. F., ... Go, D. B. (2019). The impact of transition metal catalysts on macroscopic dielectric barrier discharge (DBD) characteristics in an ammonia synthesis plasma catalysis reactor. *Journal of Physics D: Applied Physics*, *52*(22). doi:10.1088/1361-6463/ab0c58
17. Bogaerts, A., Zhang, Q., Zhang, Y., Laer, K. Van, & Wang, W. (2019). Burning questions of plasma catalysis: Answers by modeling. *Catalysis Today*, *337*, 3–14. doi:10.1016/j.cattod.2019.04.077
18. Iwamoto, M., Akiyama, M., Aihara, K., & Deguchi, T. (2017). Ammonia Synthesis on Wool-Like Au, Pt, Pd, Ag, or Cu Electrode Catalysts in Nonthermal Atmospheric-Pressure Plasma of N₂ and H₂. *ACS Catalysis*, *7*, 6924–6929. doi:10.1021/acscatal.7b01624
19. Ventura, L. R., & Fellows, C. E. (2019). The N₂ second positive (C³Π_u → B³Π_g) system reviewed: Improved data and analysis. *Journal of Quantitative Spectroscopy and Radiative Transfer*, *239*, 10–15. doi:10.1016/j.jqsrt.2019.106645
20. Mehta, P., Barboun, P., Engelmann, Y., Go, D. B., Bogaerts, A., Schneider, W. F., & Hicks, J. C. (2020). Plasma-Catalytic Ammonia Synthesis Beyond the Equilibrium Limit. *ACS Catalysis*, *10*(12), 6726–6734. doi:10.1021/acscatal.0c00684
21. Diekhöner, L., Mortensen, H., Baurichter, A., & Luntz, A. C. (2000). Coverage dependence of activation barriers: Nitrogen on Ru(0001). *Journal of Vacuum Science & Technology A: Vacuum, Surfaces, and Films*, *18*(4). doi:10.1116/1.582376
22. Dahl, S., Sehested, J., Jacobsen, C. J. H., Törnqvist, E., & Chorkendorff, I. (2000). Surface science based microkinetic analysis of ammonia synthesis over ruthenium catalysts. *Journal of Catalysis*, *192*(2), 391–399. doi:10.1006/jcat.2000.2857
23. Hammer, B., & Nørskov, J. K. (2000). Theoretical Surface Science and Catalysis — Calculations and Concepts. *Advances in Catalysis*, *45*, 71–129. doi:http://dx.doi.org/10.1016/S0360-0564(02)45013-4
24. Mortensen, J. J., Hammer, B., & Nørskov, J. K. (1998). Alkali promotion of N₂ dissociation over Ru(0001). *Physical Review Letters*, *80*(19), 4333–4336. doi:10.1103/PhysRevLett.80.4333
25. Honkala, K., Hellman, A., Remediakis, I. N., Logadottir, A., Carlsson, A., Dahl, S., ... Nørskov, J. K. (2005). Ammonia Synthesis from First-Principles Calculations. *Science*, *307*(5709), 555–558. doi:10.1126/science.1106435
26. Murphy, M. J., Skelly, J. F., Hodgson, A., & Hammer, B. (1999). Inverted vibrational distributions from N₂ recombination at Ru(001): Evidence for a metastable molecular chemisorption well. *Journal of Chemical Physics*, *110*(14), 6954–6962. doi:10.1063/1.478601
27. Diekhöner, L., Mortensen, H., & Baurichter, A. (2001). N₂ dissociative adsorption on Ru(0001): The role of energy loss. *Journal of Chemical Physics*, *115*(19), 9028–9035. doi:10.1063/1.1413746